Nano Research
2022, 15(9): 8255–8269

ISSN 1998-0124 CN 11-5974/O4
https://doi.org/10.1007/s12274-022-4462-8

Research Article

Synergistic anti-tumor therapy by a homotypic cell membrane-cloaked biomimetic nanocarrier with exceptionally potent activity against hepatic carcinoma

Shini Feng[1,§], Pinyue Ni[1,§], Yan Gong[1], Bijiang Geng[2], Hui Li[1], Chenlin Miao[1], Ruyu Fan[1], Levon Galstyan[1,3], Dengyu Pan[2], Fuxue Chen[1] (✉), and Huafei Li[1] (✉)

[1] *School of Lifesciences, Shanghai University, Shanghai 200444, China*
[2] *School of Environmental and Chemical Engineering, Shanghai University, Shanghai 200444, China*
[3] *SLAVMED Medical Center, Manandyan st., 9 bld., Yerevan 0037, Republic of Armenia*
[§] *Shini Feng and Pinyue Ni contributed equally to this work.*

Received: 1 March 2022 / **Revised:** 17 April 2022 / **Accepted:** 21 April 2022

ABSTRACT

Hepatic carcinoma (HC) is the sixth most frequently occurring malignancies and the third leading cause of cancer death worldwide. Sepantronium bromide (YM155) is a small molecule inhibitor of survivin, which has broad-spectrum anticancer therapeutic effects in various xenograft models. However, several-day continuous infusion is required to achieve greater anti-tumor efficacy because of rapid elimination from the blood circulation. Herein, a SMMC-7721 cancerous cyto-membrane-cloaked drug delivery system (DDS) (named as iM7721@GQD-YM), was developed for co-encapsulation of YM155 and graphene quantum dots (GQDs). Cytomembrane coating endowed iM7721@GQD-YM with effective targeting for homologous HC cells, excellent biocompatibility and favorable immunocompatibility for *in vivo* application. Surface decoration of iRGD peptide further enhanced its tumor targeting activity by iRGD-integrin recognition. In addition, under the irradiation of near-infrared ray (NIR), GQDs can directly kill tumors through photothermal effect and cause cell membrane rupture, accurately releasing YM155 at tumor sites. The physicochemical properties, *in vivo* and *ex vivo* anti-tumor efficacy, and mechanisms of iM7721@GQD-YM nanoparticles (NPs) were systematically investigated in this work. The experimental results clearly indicate that the versatile biomimetic DDS holds great potential for the treatment of HC, which merits further investigation in both pre-clinical and clinical studies.

KEYWORDS

hepatic carcinoma, sepantronium bromide (YM155), cancer cell membrane, biomimetic drug delivery system, graphene quantum dots, photothermal effect

1 Introduction

Hepatic carcinoma (HC) is the sixth-most frequently occurring malignancies worldwide, with approximately 906,000 new cases in 2020 [1]. China has the greatest number of cases, which is attributable to both an elevated morbidity (18.3 per 100,000) and the world's largest population [2]. Although surgical resection remains the most effective treatment, more than 80% of HC patients have entered the advanced stage at the time of diagnosis and lost the opportunity for surgery [3, 4]. Despite significant improvements in the prevention and treatment in the last decades, HC remains the third-most leading cause of cancer death according to the latest statistic report [1, 5]. Therefore, finding safe and effective therapeutic methods is urgently needed.

Survivin is an important member of the inhibitor of apoptosis (IAP) family, which is required for fetal development but later become absent in terminally differentiated tissues such as adult liver, spleen, kidney, and other visceral organs [6, 7]. However, many studies have shown that survivin is significantly overexpressed and plays vital roles in a variety of malignancies, rending it an ideal potential target for cancer therapy [8]. During the development and progression of HC, elevated expression of survivin inhibits cancer cell apoptosis, promotes proliferation, induces tumor stromal angiogenesis, and ultimately affects the prognosis of patients [9]. And inhibition of survivin could effectively promote apoptosis, reduce the survival potential of malignant cells, and enhance their sensitivity to therapeutic agents [9–11].

Sepantronium bromide (YM155) is an innovative small molecule inhibitor that acts directly on the survivin promoter region, thereby effectively inhibiting its expression at the protein level [12]. Pre-clinical studies have shown that YM155 has a broad-spectrum anticancer therapeutic efficacy in various xenograft models [13, 14]. However, as YM155 shows time-dependent activity and is rapidly eliminated from the blood circulation, greater anti-tumor efficacy should be obtained by several-day continuous infusion for achieving therapeutic concentrations in the tumor site, the method is inconvenient for both patients and healthcare professionals [15]. Thus, formulating YM155 in a

Address correspondence to Fuxue Chen, Chenfuxue@staff.shu.edu.cn; Huafei Li, huafey_lee@163.com

suitable drug delivery system (DDS) to prolong its circulation time and provide targeting to tumors would be an effective way for promoting therapeutic efficacy.

In recent years, a variety of smart nano-sized biomaterials provide more choices for drug delivery [16–18]. However, clinical application of a great many DDSs is still significantly restricted because of limited tumor targeting, premature drug leakage, and nanomaterials' prone to be engulfed by macrophages due to weak immunocompatibility, etc. [19–22]. To overcome these weaknesses, the biomimetic strategy with utilization of natural cell membrane camouflage technology has been widely employed in nano-drug preparations for tumor diagnosis and treatment [23–26]. Numerous studies have shown that adhesion molecules expressed on cancer cell membrane (CCM) can navigate and anchor cancer cells through receptor–ligand binding [27, 28]. Besides, CCM-camouflage endowing nanoparticles (NPs) with immunomodulatory self-markers, could enhance their anti-phagocytic abilities and prolong their *in vivo* circulation time [29]. To this regard, among various cytomembranes, CCM attracts our attention. We hypothesize that applying homotypic CCM as cloak could endow nanocarrier with excellent homotypic targeting ability and remarkable immunocompatibility, resulting in prominent tumor suppressing activity [30, 31].

In this study, we designed an HC membrane cloaked DDS for delivering YM155 to homotypic cancerous cells. In order for further improving its targeting ability, iRGD, which is a tumor-targeting transmembrane peptide and can be closely combined with the highly expressed αvβ3/β5 integrin on malignant cells, was modified on surface of the biomimetic DDS. Besides, a self-synthesized graphene quantum dot (GQD), which can effectively convert near-infrared ray (NIR) irradiation into heat energy, was co-encapsulated to generate the effect of photothermal therapy (PTT), directly inducing tumor cell apoptosis by thermal ablation [32, 33]. Moreover, YM155 can be effectively released due to membrane disturbance caused by the photothermal effect of GQDs, further improving the anti-tumor effects (Fig. 1).

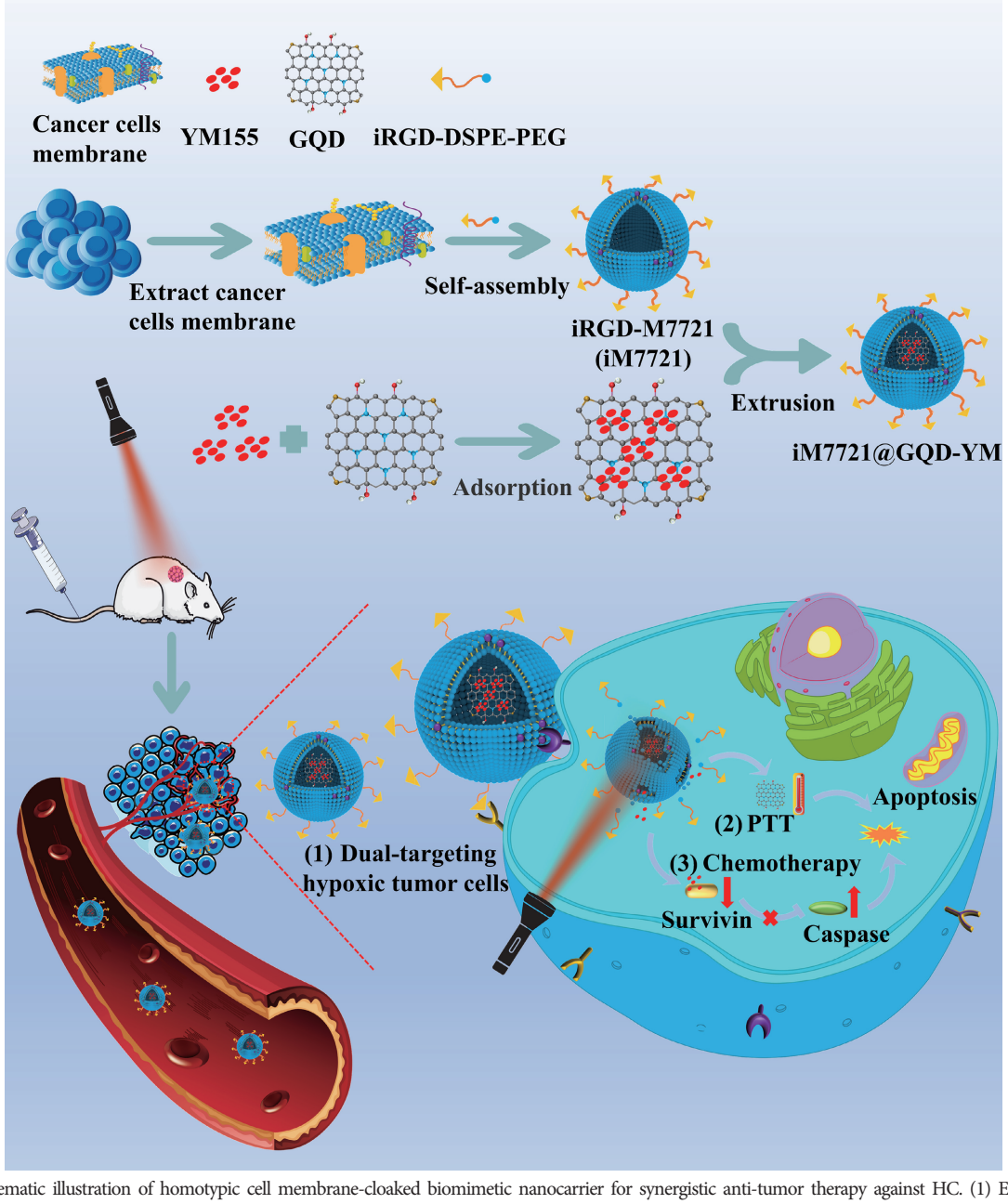

Figure 1 Schematic illustration of homotypic cell membrane-cloaked biomimetic nanocarrier for synergistic anti-tumor therapy against HC. (1) Effective tumor accumulation by homologous cell membrane recognition/iRGD-mediated synergistic targeting. (2) Under NIR radiation, GQD can directly kill tumors through photothermal therapy, and cause cell membrane rupture, accurately releasing YM155 at tumor sites. (3) Released YM155 promotes the apoptosis of tumor cells.

2 Results and discussion

2.1 Preparation and characterization of GQDs

GQD with NIR response was synthesized by one-step hydrothermal molecular fusion method (Fig. S1(a) in the Electronic Supplementary Material (ESM)). Transmission electron microscopy (TEM) images (Fig. S1(b) in the ESM) illustrate that GQDs had high dispersion in an aqueous solution with an average particle size of approximately 5.5 ± 1.4 nm. X-ray diffraction (XRD), Raman, Fourier transform infrared (FTIR) spectrometer, and X-ray photoelectron spectroscopy (XPS) results (Figs. S1(c)–S1(f) in the ESM) reveal that GQD is N-doped, abundant hydroxyl and amino functional groups which indirectly indicates its favorable water solubility [34].

The UV–visible (UV–vis) spectra (Fig. S2(a) in the ESM) show that GQD has obvious light absorption from 600 to 1,200 nm, covering the visible to near-infrared region. Fluorescence spectrum analysis (Fig. S2(b) in the ESM) shows that the optimal excitation and emission wavelength of GQD are 405 and 480 nm, respectively. When the excitation wavelength changes from 300 to 420 nm, the position of the fluorescence emission peak (photoluminescence (PL)) remains unchanged, indicating no fluorescence excitation wavelength dependence of GQD (Fig. S2(c) in the ESM). Confocal laser scanning microscopy (CLSM) results indicate that when GQD was endocytosed into cells, the bright green fluorescence signal can be observed, and the fluorescence intensity did not significantly decrease after continuous NIR irradiation for 30 min (Fig. S2(c) in the ESM). Figures S2(d)–S2(f) in the ESM indicate that after NIR irradiation, the temperature of GQD solution significantly increased in both concentration and power dependent manners, and the temperature rise efficacy was rarely affected after six consecutive on/off laser irradiation, indicating its excellent photothermal stability. In addition, we measured the heating and cooling curves of 300 μg/mL GQD under NIR irradiation with a power density of 0.8 W/cm^2, and the photothermal conversion efficiency (η) of GQD was calculated to be as high as 52.4% (Figs. S2(g)–S2(i) in the ESM), similar to the same products employed in our previous study [35].

2.2 Characterization of biomimetic NPs

To prepare biomimetic NPs, we firstly extracted the cytomembrane of SMMC-7721 cells, and then wrapped GQD and YM155 (GQD/YM) by liposome squeezer. TEM and scanning electron microscopy (SEM) images (Figs. 2(a) and 2(b)) show that iM7721@GQD-YM (stands for iRGD-M7721@GQD-YM) is uniform and stable spherical, with an ideal particle size of approximately 100 nm, in accordance with the dynamic light

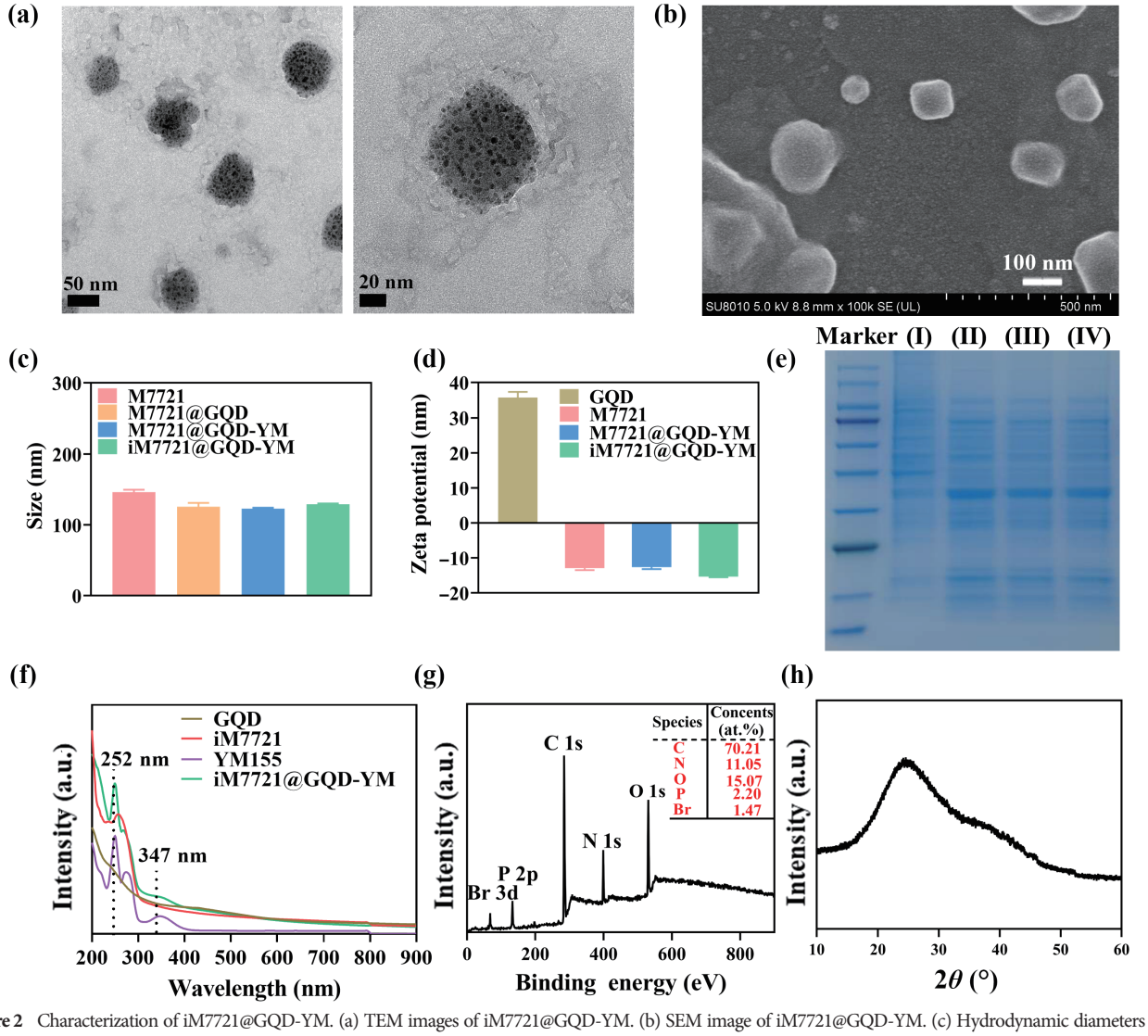

Figure 2 Characterization of iM7721@GQD-YM. (a) TEM images of iM7721@GQD-YM. (b) SEM image of iM7721@GQD-YM. (c) Hydrodynamic diameters and (d) zeta potential of iM7721@GQD-YM and counterparts. (e) SDS-PAGE for different samples ((I): cancer cell lysate, (II): cancer cell empty vesicles, (III): M7721@GQD-YM, (IV): iM7721@GQD-YM). (f) UV–vis absorption, (g) XPS spectrum, and (h) XRD pattern of iM7721@GQD-YM.

scattering (DLS) results (Fig. 2(c)). Moreover, dot-like particles can be seen within the vesicles, directly indicating the successful encapsulation of GQDs. Figure 2(d) reveals that the zeta potential of GQD altered from positive (35.7 ± 1.6 mV) to negative after being coated into negatively charged cytomembranes. The surface protein library of bionic NPs from source cells was determined by sodium dodecyl sulfate-polyacrylamide gel electrophoresis (SDS-PAGE) (Fig. 2(e)), the results of which show similar protein composition among cancer cell lysates (I), empty cancer cell vesicles (II), M7721@GQD-YM (III), and iM7721@GQD-YM (IV). Successful encapsulation of YM155 was validated by UV–vis spectra analysis, and the results show that iM7721@GQD-YM owns remarkable absorption at 252 nm, being present in the results of YM155 but absent in that of both cytomembrane (iM7721) and free GQD (Fig. 2(f)). Similarly, encapsulation of GQD was validated by XPS spectrum (Fig. 2(g)), the results of which reveal that P and Br are present in iM7721@GQD-YM but absent in free GQD. Besides, Fig. 1(h) indicates that XRD pattern of iM7721@GQD-YM is similar to that of free GQD (Fig. S1(c) in the ESM), indicating the crystal structure of GQD was not affected during the process of encapsulation.

2.3 *In vitro* stability, photothermal properties, and drug release

Considering the intended use (intravenous administration), phosphate buffered saline (PBS) and Dulbecco's modified Eagle's medium (DMEM) containing 50% fetal bovine serum (FBS) was employed as *in vitro* serum models to check the particle serum stability [36]. The existence of FBS was employed to mimic a variety of serum proteins in the complicated environment within the blood vessels. Figure 3(a) shows no obvious size alteration of iM7721@GQD-YM during the experimental period of 6 days in both PBS buffer and DMEM culture, regardless of whether FBS is added to the solution, indicating a high stability of the biomimetic system. Figure 3(d) reveals that after co-incubation with SMMC-7721 cells, the fluorescence signal of GQD (green) was co-localized with the membrane signal (red), indicating that iM7721@GQD-YM could well maintain its structural integrity even after a short period of cellular uptake.

To explore the photothermal properties, different samples were treated with irradiated with NIR (808 nm, 1.0 W/cm^2, 5 min), and the temperature was measured and recorded by Fluke infrared thermal imager. As shown in Figs. 3(b) and 3(c), no obvious temperature variation of empty cytomembrane (M7721) was observed after irradiation. However, free and encapsulated GQDs showed a sharply temperature increase, reaching to approximately 56.1 and 54.4 °C respectively. It seems that although encapsulated GQDs displayed a slower temperature rise than free ones, effective and excellent photothermal abilities still retain for encapsulated GQDs, meeting the requirements for subsequent application.

It was well expected that our bionic DDS could be an excellent drug carrier, benefiting from the natural and stable structure. For validating this expectation, we evaluated the YM155 encapsulation efficiency (EE) and release profile. Figure 3(e) reveals that when original YM155 increased to 500 μg/mL, the EE of M7721@GQD-YM and iM7721@GQD-YM were calculated to be as high as 79.03% and 79.75%, respectively. Figure 3(f) demonstrates that iM7721@GQD-YM exhibits a sustained drug release in neutral (pH = 7.4) environment, with no initial burst during the period of 72 h. The release rate significantly accelerated under acidic conditions (pH = 5.0). This is because that lower pH increases the extent of protonated phosphatidic acid (PA) headgroups on membrane bilayer lipids and PA-rich heterogeneities, giving rise to molecular packing defects originating at the phase boundaries [37]. It is also acknowledged that cytomembranes consist of bilayer lipids embedded with transmembrane proteins, whose formation and dynamic properties are temperature-dependent. At sufficiently high temperature, the molecular kinetic energy constituting the cell membrane is greater than the binding force that maintains the cell membrane formation, leading to the

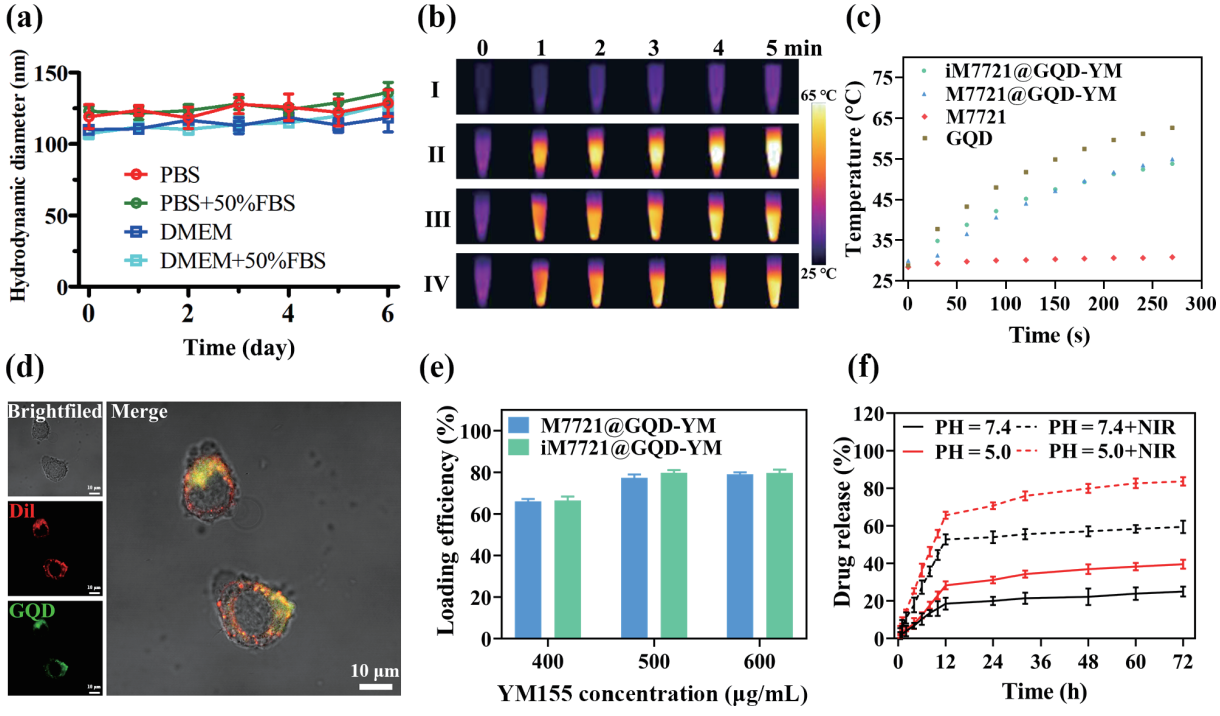

Figure 3 Serum stability, drug loading, and releasing profiles of the biomimetic DDS. (a) Excellent *in vitro* serum stability of iM7721@GQD-YM. (b) Infrared thermal images of I: iM7721; II: GQD; III: M7721@GQD-YM; and IV: iM7721@GQD-YM with NIR laser irradiation. (c) Temperature curves of different agents under NIR laser irradiation for 5 min. (d) CLSM image of SMMC-7721 cells after co-culture with iM7721@GQD-YM (red: fluorescence signal of Dil-labeled membrane; green: fluorescence signal of GQD). (e) Encapsulation efficiency of M7721@GQD-YM and iM7721@GQD-YM. (f) Drug release profile of YM155 from biomimetic DDS at different conditions.

dissociation of the lipid bilayer [38]. This so-called temperature responsive drug release was also validated in Fig. 3(e), the results indicate that NIR irradiation can enhance the membrane permeability, with more than 50% encapsulated YM155 being released after 12 h. All these results reveal that iM7721@GQD-YM could maintain stability under physiological conditions and release drugs rapidly of cancer cells in the acidic environment. Moreover, we can also effectively regulate the release of drugs by NIR irradiation at desired sites, thereby reducing the side effects of containing therapeutics [39, 40].

2.4 Excellent *in vitro* biocompatibility

Hemocompatibility was examined by incubating erythrocytes with iM7721@GQD-YM and counterparts at gradient concentrations. As indicated in Figs. 4(a) and 4(b), free and encapsulated GQDs all exhibit moderate hemolysis rate (less than 7%) at different concentrations (from 25 to 400 μg/mL). Besides, both free and encapsulated GQDs demonstrate low-cytotoxicity to four different cells (including LO2, HepG2, SMMC-7721, and PATU-8988) in concentrations of up to 400 μg/mL (Figs. 4(c) and 4(d)). These results clearly reflect that iM7721@GQD and counterparts own excellent biocompatibility.

2.5 Favorable immunocompatibility

It is well established that artificial NPs can be easily recognized and eliminated by the reticuloendothelial system (RES), resulting in limited circulation time and insufficient accumulation in tumor sites [41]. However, cancer cells, which were employed for particle camouflage in this study, have the ability to avoid the recognition of the immune system [42, 43]. In order to evaluate the immunocompatibility, biomimetic NPs and counterparts were incubated with J774A.1 macrophages, and swallowed GQD fluorescent was compared. As shown in Fig. 5, HC cytomembrane encapsulated GQDs are less prone than free ones to be engulfed by macrophage cells, resulting in decreased fluorescence in J774A.1 cells. Hence, it demonstrates that coating therapeutic agents with cancer cell membranes could effectively inhibit the macrophage uptake, endowing the biomimetic DDS with excellent immunocompatibility.

2.6 Enhanced intracellular uptake

We subsequently investigated the homologous targeting ability of cancer membrane camouflage. Figure 6(a) and Fig. S3(a) in the ESM demonstrate that the green fluorescence derived from free GQD incubated cells was negligible for both normal and malignant liver cells. The cytomembrane camouflage significantly enhanced the intracellular uptake of encapsulated GQDs for homologous cancerous cells (HepG2 and SMMC-7721), which indicated by increased intracellular green fluorescence intensity. In addition, iRGD decoration further enhanced the intracellular fluorescence at the same condition. However, such homologous targeting trend was not observed in normal LO2 cells. Besides, M8988 cytomembrane (a type of pancreatic cancer cell membrane employed as a nonhomologous control) enhanced cellular uptake of encapsulated GQDs is less obvious than that enhanced by homologous membrane (Fig. 6(b) and Fig. S3(b) in the ESM).

These results show that due to the homologous targeting, cytomembrane coated NPs can reach homologous cancer cells

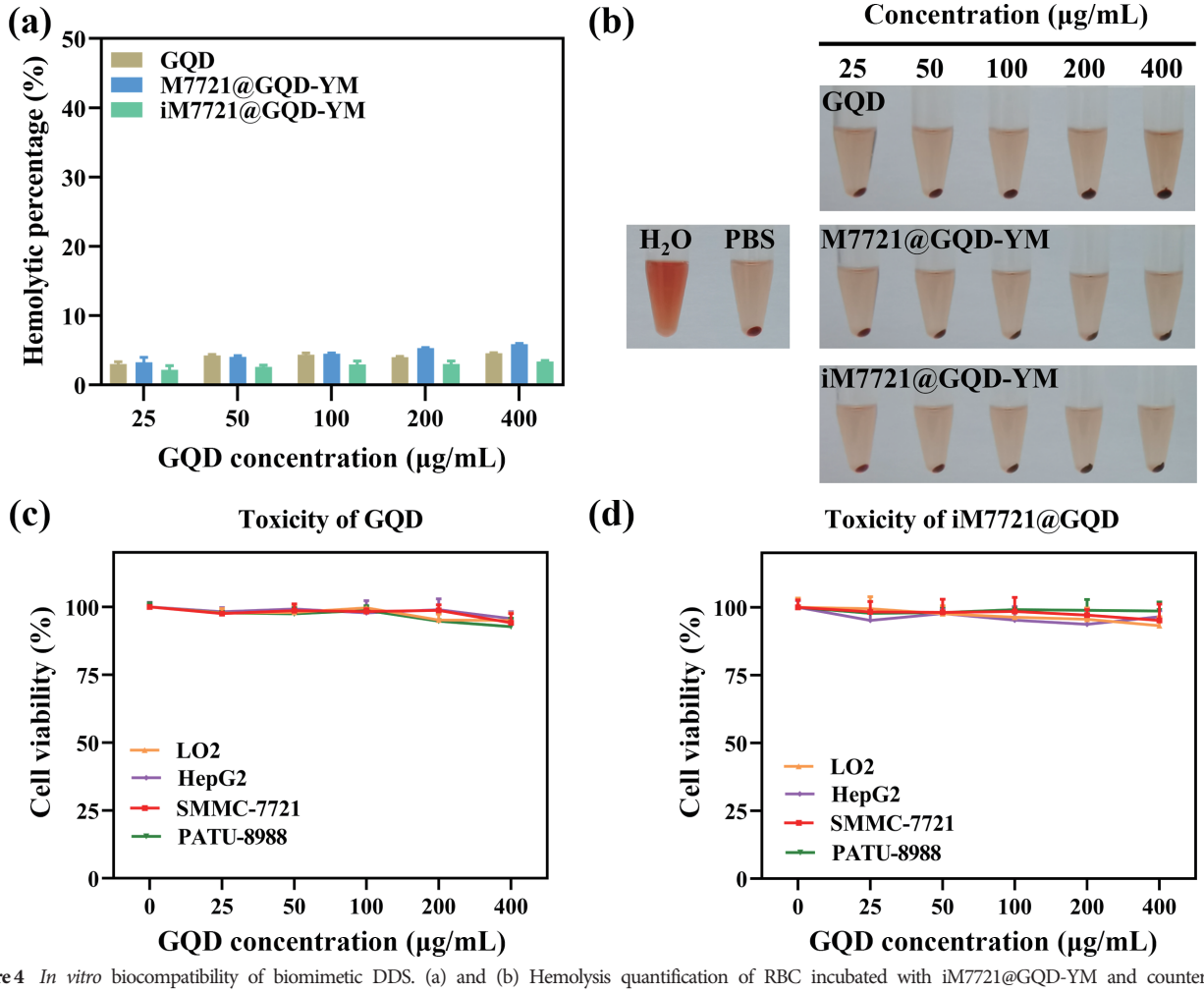

Figure 4 *In vitro* biocompatibility of biomimetic DDS. (a) and (b) Hemolysis quantification of RBC incubated with iM7721@GQD-YM and counterparts. Cytotoxicity profile of (c) GQD and (d) iM7721@GQD to various cell lines.

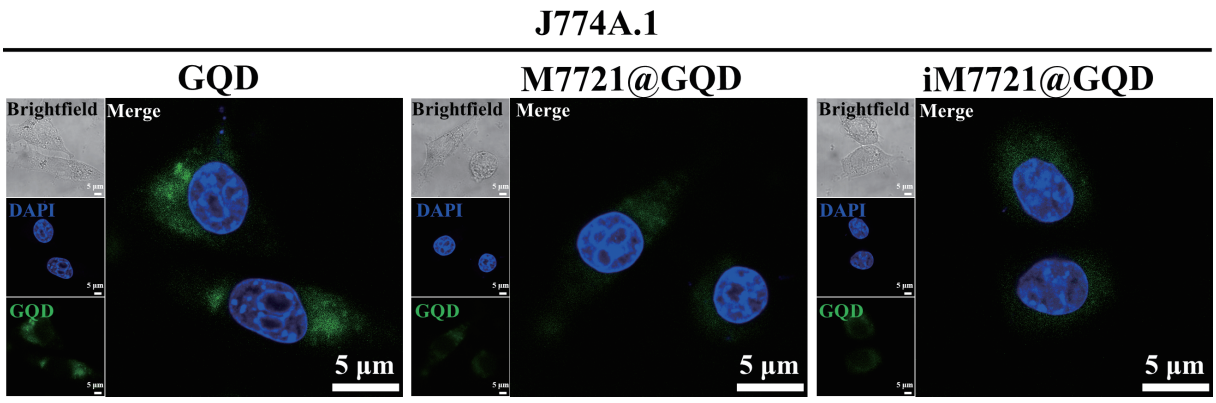

Figure 5 CLSM images of J774A.1 macrophages incubated with free and encapsulated GQDs for 2 h. Green and blue fluorescence indicates GQD and nucleus, respectively.

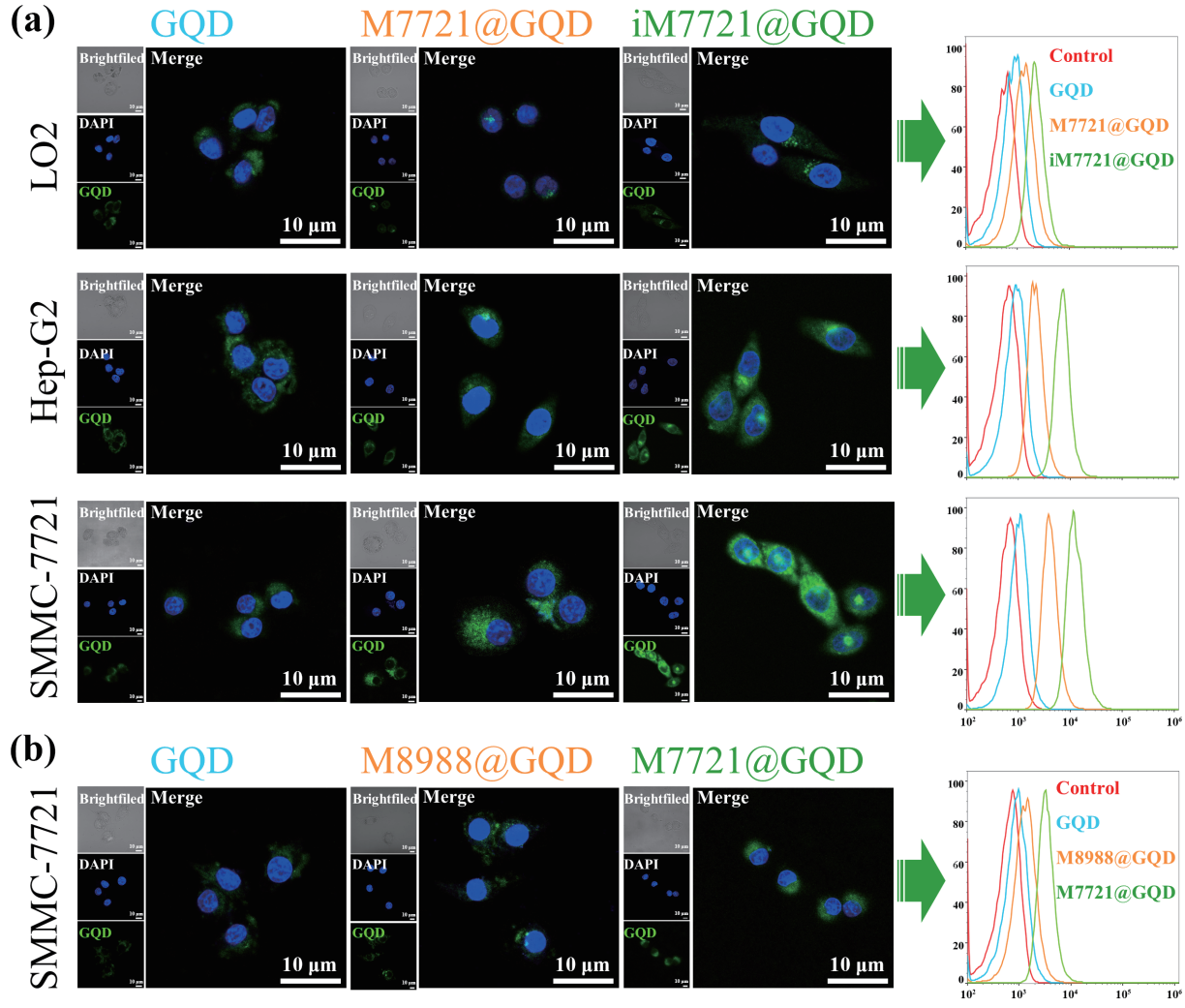

Figure 6 Cellular uptake of biomimetic DDS. (a) Effects of homologous cytomembrane and iRGD decoration on the intracellular uptake of GQDs in normal (LO2) and homologous malignant liver cells (SMMC-7721 and HepG2) by CLSM and FCM. (b) Effects of homologous and nonhomologous cytomembrane camouflaging on intracellular uptake of GQDs in SMMC-7721 cells by CLSM and FCM. Green: GQD; blue: nucleus.

more accurately. In addition, using iRGD modification further improves the penetration efficiency via it's binding with αvβ3/β5 integrin on malignant cells [44]. Therefore, the combined application of cancer cell membrane camouflage and iRGD modification has the ability of synergistic targeting, further improving the drug delivery efficiency and accuracy.

2.7 *In vitro* cytotoxicity

As illustrated in Figs. 7(a) and 7(b), both SMMC-7721 and HepG2 cells showed a significantly lower cell viability after the treatment of encapsulated drugs than free ones, while iRGD decoration slightly increased the tumor suppressing activity in all tested concentrations. More importantly, NIR irradiation further enhanced the anti-tumor effects when compared with non-irradiated groups. Furthermore, the half maximal (50%) inhibitory concentration (IC50) of YM155 was calculated to evaluate the cytotoxicity of different formulations according to the YM155 concentration dependence of cell viability. It was shown in Table 1 that when compared with non-irradiated counterparts (iM7721@GQD-YM group, $IC50_{HepG2} = 2.56$ μg/mL, $IC50_{SMMC\text{-}7721} =$

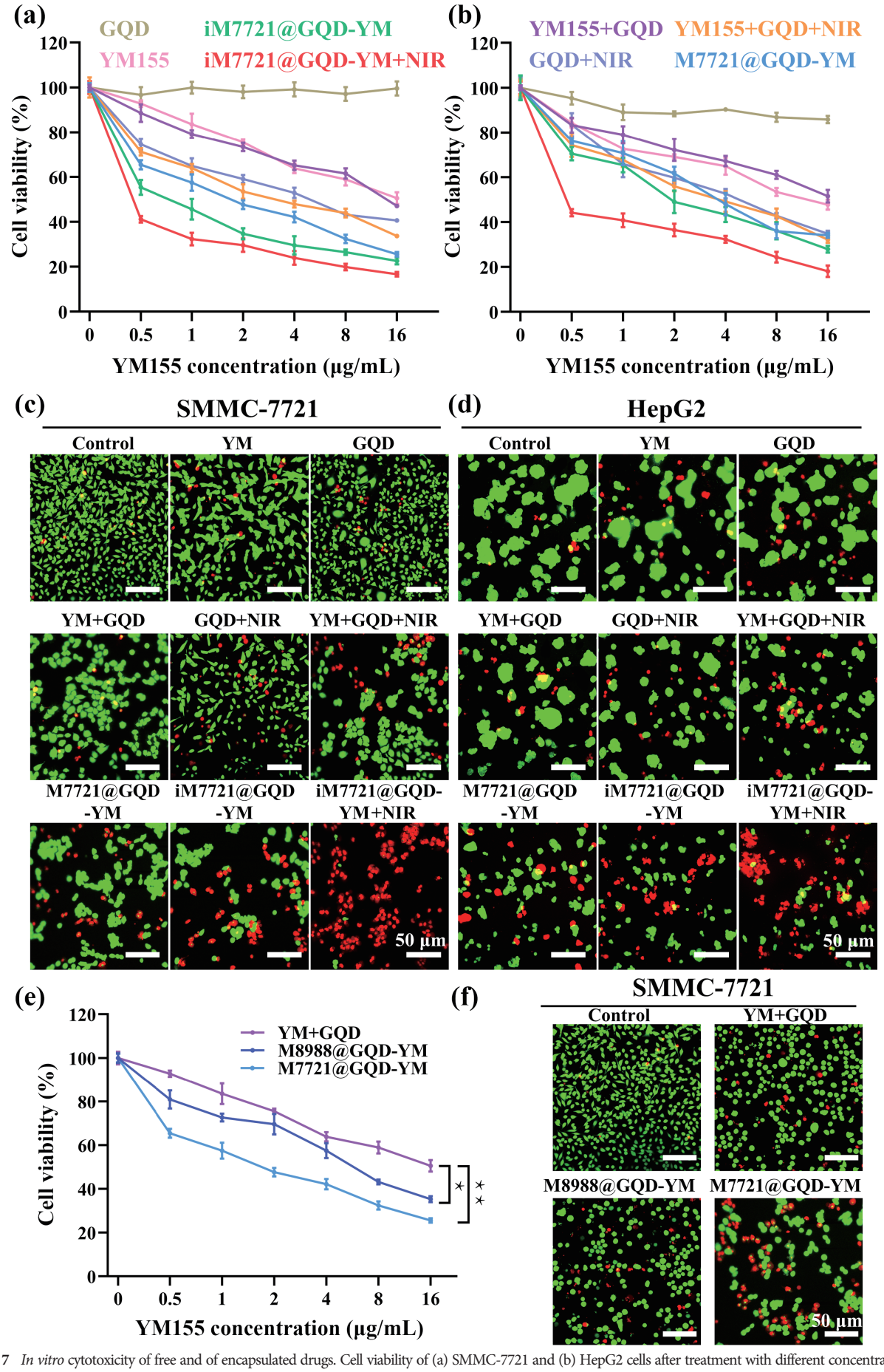

Figure 7 *In vitro* cytotoxicity of free and of encapsulated drugs. Cell viability of (a) SMMC-7721 and (b) HepG2 cells after treatment with different concentrations of free and encapsulated agents by CCK-8 analysis. Live/dead staining of SMMC-7721 (c) and HepG2 (d) cells with different treatments. The live cells were stained with calcein-AM (green) and dead cells with PI (red). Cell viability of SMMC-7721 cells after being treated with different concentrations of YM+GQD, M8988@GQD, and M7721@GQD for 24 h by CCK-8 analysis (e) and live/dead cell staining (f). Data expressed as means ± sd. $^{*}P < 0.05$; $^{**}P < 0.01$.

Table 1 IC50 (μg/mL) of free and encapsulated YM155 to HC cells

Groups	SMMC-7721 cells	HepG2 cells
YM	9.88	10.20
YM+GQD	9.73	10.33
YM+GQD+NIR	3.28	3.57
M8988@GQD-YM	5.26	5.30
M7721@GQD-YM	2.05	3.68
iM7721@GQD-YM	1.04	2.58
iM7721@GQD-YM+NIR	0.56	0.84

1.04 μg/mL), iM7721@GQD-YM+NIR group demonstrated lower IC50 to both SMMC-7721 (0.56 μg/mL) and HepG2 (0.84 μg/mL) cells, which was approximately 17 and 12 times lower than that of free drugs (YM155+GQD), respectively. Interesting, the cytotoxicity of YM155 promoted by M8988 cytomembrane was not so obvious as that promoted by homologous SMMC-7721 cytomembrane (Fig. 7(e)). All these results were validated by live-dead cell staining as shown in Figs. 7(c), 7(d), and 7(f), which further confirmed that homologous targeting, iRGD decoration, and NIR irradiation together enhanced the *in vitro* cytotoxicity of YM155 against HC cells.

2.8 Enhanced apoptosis inducing activity

As YM155 is a type of surviving suppressor, which is associated with cellular apoptosis (Fig. S4 in the ESM), we subsequently investigated the apoptosis inducing ability of our bionic DDS. As shown in Figs. 8(a) and 8(b), HC cell membrane camouflage can significantly promote the apoptosis inducing ability of encapsulated agents against two malignant cells, and this apoptosis inducing activity can be slightly enhanced by iRGD decoration in SMMC-7721 cells. Encouragingly, NIR irradiation further enhanced the cellular apoptosis, with a highest apoptosis ratio among groups (SMMC-7721 cells: 77.6%, HepG2 cells: 63.5%). Figure 8(e) and Fig. S5 in the ESM demonstrates that both cytomembrane encapsulation and NIR irradiation can enhance the biological function of YM155, including the downregulation of survivin and activation of caspase-3/9 (indicated by the upregulation of cleaved caspase-3/9). These results were validated by biological electron microscopy, as shown in Fig. 8(f). Just as expected, the apoptosis inducing ability of YM155 promoted by nonhomologous M8988 cytomembrane was not so obvious as that promoted by homologous SMMC-7721 cytomembrane (Figs. 8(c) and 8(d)).

In summary, we can draw the conclusion that our biomimetic NPs own prominent ability for enhancing the *in vitro* anti-tumor efficacy of containing drugs, which indicated by decreased cell growth and increased cellular apoptosis. This might be attributed to the co-effects of particle enhanced cellular endocytosis, homologous targeting by HC cytomembranes, and active targeting by iRGD-integrin recognition between biomimetic DDS and target cells. Besides, NIR irradiation induced local drug release and PTT may also participate in the promotion of tumor suppressing activity.

2.9 *In vivo* pharmacokinetics and biological distribution

Before evaluating the *in vivo* anti-tumor efficacy, the pharmacokinetics (PK) assays were performed to verify the long-term stability of the cancer cell membrane-cloaked DDS and encapsulated drugs. A one-compartment model was used to describe the time course of the blood YM155 concentrations [45]. As shown in the concentration–time curve (Fig. S6 in the ESM) and PK parameters (Table 2), the elimination half-time ($t_{1/2}$) of free YM155 is much shorter (0.69 h) than that of encapsulated YM155 (4.79 h). The prolonged $t_{1/2}$ of approximately 7 times directly demonstrated that the elimination of iM7721@YM was much slower than free YM155 from rat peripheral blood.

The *in vivo* distribution of free and encapsulated drugs in tumor bearing mice was investigated by *in vivo* fluorescence imaging during 72 h after intravenous injection. As we can see, the tumor accumulation of DiD fluorescence, which was employed to label the particle membrane, increased during the first 9 h, and then gradually decreased with time (Fig. 9(a)). 72-h post injection, the DiD fluorescence in the tumor region is much stronger in M7721@GQD group than those in M8988@GQD group, proving the effective target ability and enrichment effect of homologous than nonhomologous cytomembrane. Besides, the tumor fluorescence intensity in iM7721@GQD group was the highest among groups. After 72 h of injection, the nude mice were sacrificed, and main organs and tumors were taken for fluorescence imaging. Similar results further confirmed that the accumulation of dual-targeted iM7721@GQD in tumors was the most among groups (Fig. 9(b)).

To prove that GQD still owns an obvious photothermal effect *in vivo*, we monitored the temperature alteration of tumor sites during NIR irradiation. As shown in Fig. 9(c), compared with the PBS group, local temperature of tumor sites in free GQD and M8988@GQD groups slightly increased after NIR irradiation. While in the groups of homologous membrane encapsulated GQDs (M7721@GQD and iM7721@GQD), tumor sites experienced a faster and more remarkable temperature rise, with iM7721@GQD demonstrates the most excellent *in vivo* photothermal ability among groups due to the synergistic targeting effect of enhanced permeability and retention (EPR) effect, homologous cell membrane targeting, and iRGD mediated active targeting.

2.10 *In vivo* anti-tumor efficacy

The SMMC-7721 subcutaneous tumor model was employed to evaluate the *in vivo* tumor suppressing efficacy. Figures 9(d)–9(f) indicates that mice treated with free YM155+GQD exhibit rapid tumor growth and short survival, being similar to those treated with PBS. NIR irradiation slightly promotes the anti-tumor effects of free drugs, indicating that GQD's photothermal effect itself has certain ability to kill tumor cells. An obviously enhanced therapeutic effect was found for homologous cytomembrane encapsulated drugs, which was further promoted by iRGD fabrication, indicating that both cytomembrane camouflage and iRGD mediated targeting do work *in vivo*. As expected, among all experimental groups, iM7721@GQD-YM+NIR group exhibits the most outstanding tumor suppressing activity, which indicated by approximately 70% reduction of tumor volume (vs. control group) and all mice's survival at the end of survival analysis (40 days post tumor implantation). Consistently, through histological analysis, a

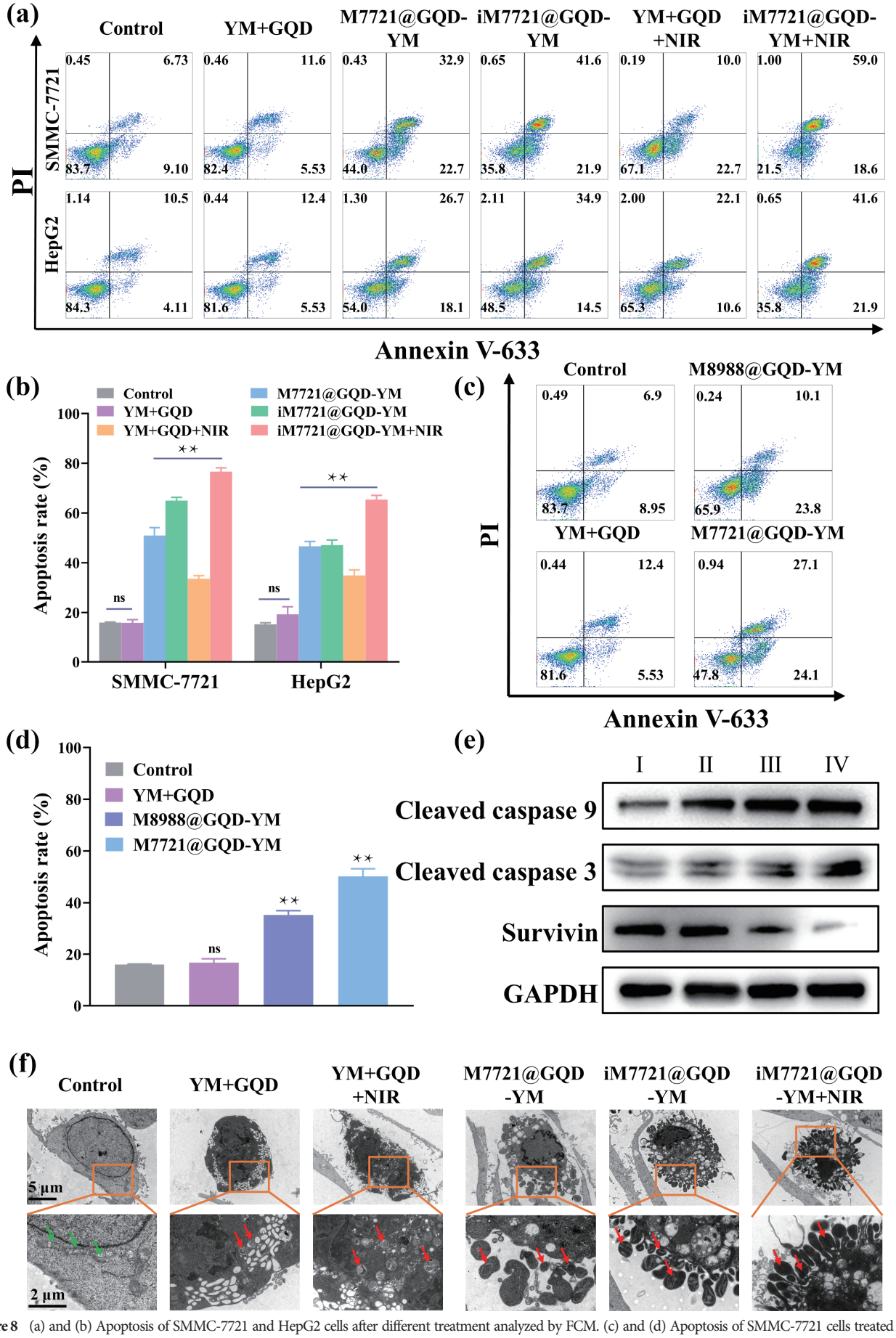

Figure 8 (a) and (b) Apoptosis of SMMC-7721 and HepG2 cells after different treatment analyzed by FCM. (c) and (d) Apoptosis of SMMC-7721 cells treated with PBS, YM+GQD, M8988@GQD-YM, and M7721@GQD-YM analyzed by FCM. (e) Western blotting analysis of cleaved caspase-9/3 and survivin in SMMC-7721 cells being treated with I: PBS; II: YM+GQD; III: iM7721@GQD-YM; IV: iM7721@GQD-YM+NIR. (f) Bio-TEM images of SMMC-7721 cells after different treatments. Lower rows were at higher magnifications of the squared areas in each upper row. The green and red arrows indicated the mitochondria and apoptosis bodies, respectively. Data expressed as means ± sd. $^{**}P < 0.01$.

Table 2 Parameters of pharmacokinetics for different formulations of YM155[a]

Groups	$t_{1/2}$ (h)	CL (L/h)	MRT (h)	$AUC_{0-\infty}$ (ng/(mL·h))
YM155	0.69	0.20	1.00	4,883.29
iM7721@YM	4.79	0.03	6.91	33,073.03

[a]Abbreviations: $t_{1/2}$: elimination half-life; CL: clearance; MRT: mean residence time; and AUC: extrapolated area under the curve from zero to infinity.

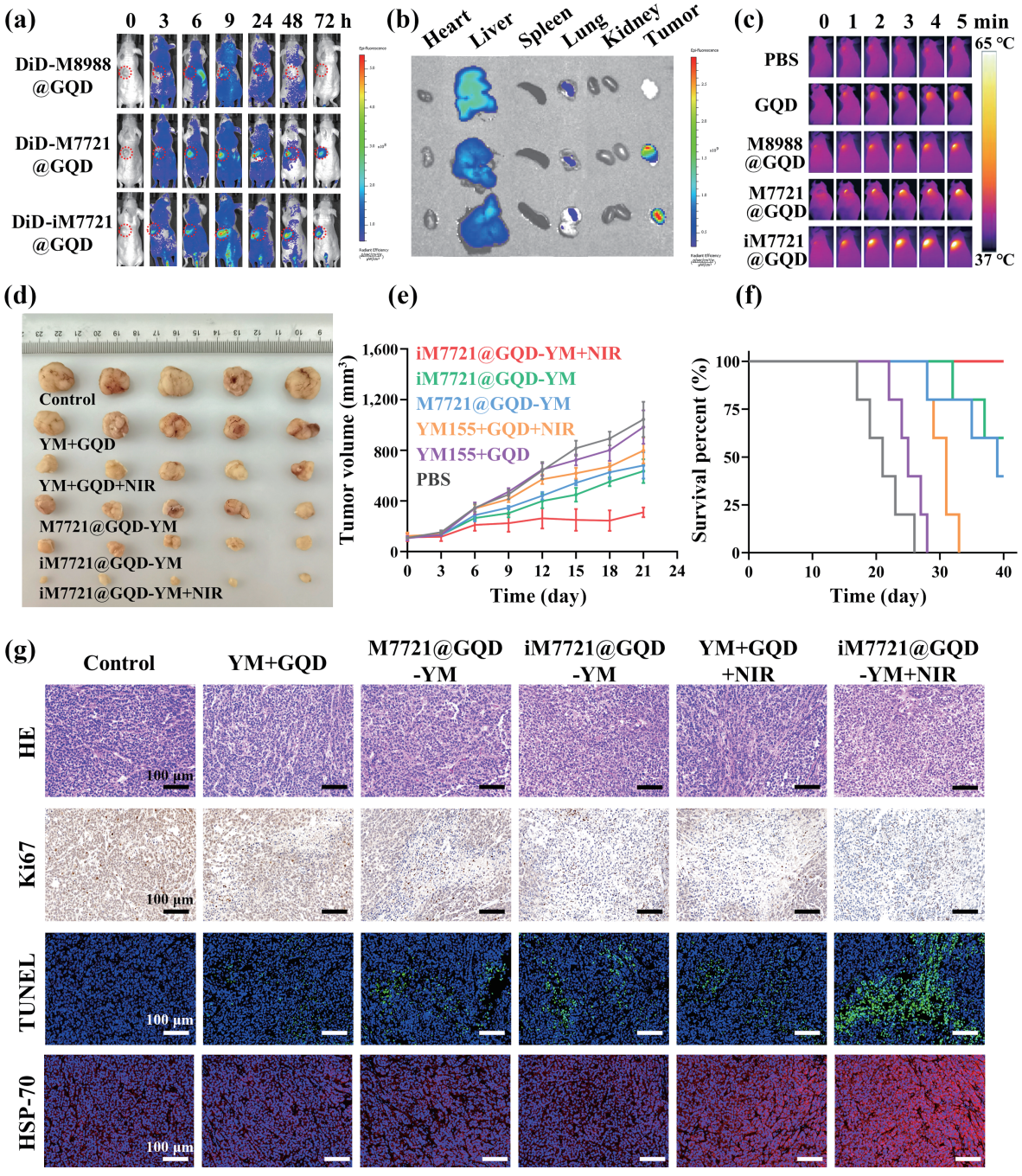

Figure 9 *In vivo* antitumor efficacy of the biomimetic DDS. (a) Fluorescence imaging of tumor-bearing mice after intravenous injection of DiD-M8988@GQD, DiD-M7721@GQD, and DiD-iM7721@GQD. (b) Fluorescence imaging of major organs and tumors from nude mice 72 h after injection of DiD-M8988@GQD, DiD-M7721@GQD, and DiD-iM7721@GQD. (c) Infrared thermal images of tumor bearing mice with different treatment under NIR irradiation. (d) Representative photographs of tumors collected from mice of various groups 21 days after treatment. (e) Quantitative results of the SMMC-7721 tumor volumes after different treatments during the experimental course ($n = 6$). (f) Survival curves of SMMC-7721 tumor-bearing nude mice treated with different formulations. (g) H&E staining, immunohistochemical staining with Ki67, immunofluorescence staining with HSP70 and TUNEL assay of tumor tissues. Data expressed as means ± sd. $^{**}P < 0.01$.

more marked reduction of tumor cells, lower Ki67 staining, and remarkable terminal deoxynucleotidyl transferase mediated dUTP nick-end labeling (TUNEL) signaling in iM7721@GQD-YM+NIR treated tumors were detected than others (Fig. 9(g)).

During the clinical application of anti-cancer drugs, the main side effects of anti-cancer drugs are due to their cumulative and dose-dependent hematotoxicity, hepatotoxicity, and nephrotoxicity. Thus, blood routine and biochemical indexes in plasma taken from tumor bearing mice were measured 24 h after therapeutic agent injection to evaluate their *in vivo*

biocompatibility. As we can see, the counts of white blood cell (WBC) and platelet (PLT) decreased, and blood aspartate transaminase (AST), urea nitrogen (UREA), creatinine (CREA) increased slightly in mice treated with free drugs. However, there are no significant differences between the biomimetic DDS treated groups and the PBS control group in both blood routine and biochemistry indexes (Figs. S7 and S8 in the ESM). The hematoxylin and eosin (H&E) staining assay also indicated the minimal systematic toxicity of encapsulated drugs (Fig. S9 in the ESM).

These results confirmed that our bionic DDS was characterized of low toxicity, excellent biocompatibility, and satisfactory therapeutic efficiency in tumor bearing mice, which could be used as an effective nano-platform for photothermal/chemotherapy combined therapy.

2.11 Immunogenic cell death induced by the treatment of biomimetic DDS

Figure 9(g) illustrates that the heat shock protein 70 (HSP70) was found to be remarkably upregulated in tumor tissues following NIR irradiation (YM+GQD+NIR and iM7721@GQD-YM+NIR experimental groups). HSP constitutes a class of chaperones, which function to protect cells by refolding damaged proteins or by redirecting them to proteasomal degradation under non-lethal stress conditions [46]. HSP70 can translocate from intracellular compartments to cell surface during certain types of cell death, facilitating the uptake of tumor associated antigens (TAAs) by antigen presenting cells (APCs), and hence can elicit an antigen-specific immune response against a broad spectrum of solid tumors [47]. This so-called immunogenic cell death (ICD) was also characterized and accompanied by a variety of danger associated molecular patterns (DAMPs) such as calreticulin (CRT), high mobility group box 1 (HMGB-1), adenosine triphosphate (ATP), and TAAs etc. [47]. In order to verify whether the biomimetic is an effective ICD inducer, we performed experiments for evaluating the expression of CRT, and HMGB1/ATP release in SMMC-7721 cells treated by iM7721@GQD-YM and counterparts. CRT plays the most important roles in promoting ICD induced antitumor response, which binds to CD91 receptors on dendritic cells (DCs), enabling phagocytosis of dying cancer cells as well as antigen cross-presentation to cytotoxic T lymphocytes [48]. As we can see from Figs. 10(a)–10(c), upregulated CRT expression can be found on surface of cells treated with NIR irradiation (YM+GQD+NIR and iM7721@GQD-YM+NIR experimental groups). In accordance, promoted releases of HMGB1 and ATP, which are two major hallmarks of ICD, were also detected in the supernatant of NIR treated cells (Figs. 10(d) and 10(e)). A variety of studies illustrated that fever-like local temperature induced by PTT can efficiently induce the ICD against malignant cells via the enhanced antigen presentation, improved tumor blood flow, and accelerated leukocyte trafficking in tumor microenvironment [49]. This may explain the upregulation of ICD hallmarks in NIR irradiated tumor tissues and cells illustrated in Figs. 9 and 10.

3 Methods

3.1 Materials and cells

4',6-Diamidino-2-phenylindole (DAPI) nuclear staining solution, 4% paraformaldehyde, and Coomassie brilliant blue were obtained from Beyotime Biotechnology (Shanghai, China). AM/PI cell double staining kit and Annexin V-633/PI cell apoptosis kit were bought from Dojindo (Kumamoto, Japan). YM155 was provided by Sigma-Aldrich (MO, USA). DSPE-PEG-iRGD was purchased from MeloPEG (Shanghai, China). Two human liver cancer cell lines (SMMC-7721 and HepG2), human normal liver cell line (LO2), human pancreatic cancer cell line (PATU-8988), and mouse mononuclear macrophage cell line (J774A.1) were all obtained from the American Type Culture Collection (ATCC, Manassas, VA, USA). Cells were incubated in DMEM containing 10% (v/v) FBS and 1% penicillin/streptomycin (Thermo Fisher Scientific, Massachusetts, USA) in a humidified incubator at 37 °C with 5% CO_2.

3.2 Preparation of GQD

GQDs were prepared according to our previous publication [50]. Briefly, 1,3,6-trinitropyrene (TNP) was first prepared through the nitration reaction of pyrene (TCI, Japan). With TNP as the precursor, 0.1 g TNP and 0.8 g polyethyleneimine (BPEI) were mixed and dissolved in 10 mL deionized water. After adequately mixing, the solution was placed in a reactor and reacted at 230 °C for 12 h. The products obtained by microwave were filtered by a 0.22 μm aqueous membrane, and the unreacted reactants were removed. The black powder (GQDs) was obtained by freeze-drying.

3.3 Cell membrane extraction

Cancer cell membrane was extracted as previously described [27, 51]. Briefly, cultured cells were collected, washed, and finally resuspended in PBS to maintain the cell density at about 10^7/mL. The well-prepared lysate containing sodium bicarbonate and ethylene diamine tetraacetic acid (EDTA) were added to the suspension, and phenylmethylsulfonyl fluoride (PMSF) was then added to prevent membrane protein degradation. The mixture was placed in a refrigerator at 4 °C overnight. The lysed cells were crushed by sonication (80 W, 10 min) and centrifuged (3,200*g*, 5 min). The supernatant was collected and centrifuged (100,000*g*, 30 min), and the precipitate was collected, which resuspended in PBS and stored at −80 °C for future use.

3.4 Encapsulation of GQD and YM155 in biomimetic DDS

The GQDs (800 μg/mL) and YM155 (800 μg/mL) were mixed and subjected to ultrasonic oscillation for 4 h. Subsequently, extracted cell membrane was added, and the mixture was then extruded through polycarbonate films with pore sizes of 400 and 200 nm for 30 cycles to obtain NPs with uniform size. For the preparation of iRGD decorated NPs, cancer cell membranes (CCMs) were incubated with DSPE-PEG-iRGD at 37 °C for 30 min and then ultrasonically suspended for 30 s before being added to GQD/YM155 solution.

3.5 Cell membrane integrity analysis

The membrane protein characterization was conducted by SDS-PAGE [52]. Specifically, samples were prepared with 1 mg/mL final protein concentration in the loading buffer and heated in a metal bath for 10 min. The samples (20 μL) were subjected to SDS-PAGE, and protein bands were stained by using Coomassie blue before imaging.

3.6 Particle characterization

For the preparation of specimens for TEM measurement (Emesis Veleta G3 transmission electron microscope) experiments, the droplet containing GQD or iM7721@GQD-YM was placed on Holey Carbon Coated-Copper 200 mesh Grids (Ted Pella, California, USA). Samples were examined on TEM at 80 kV after air-dried. The photothermal conversion efficiency of NP was

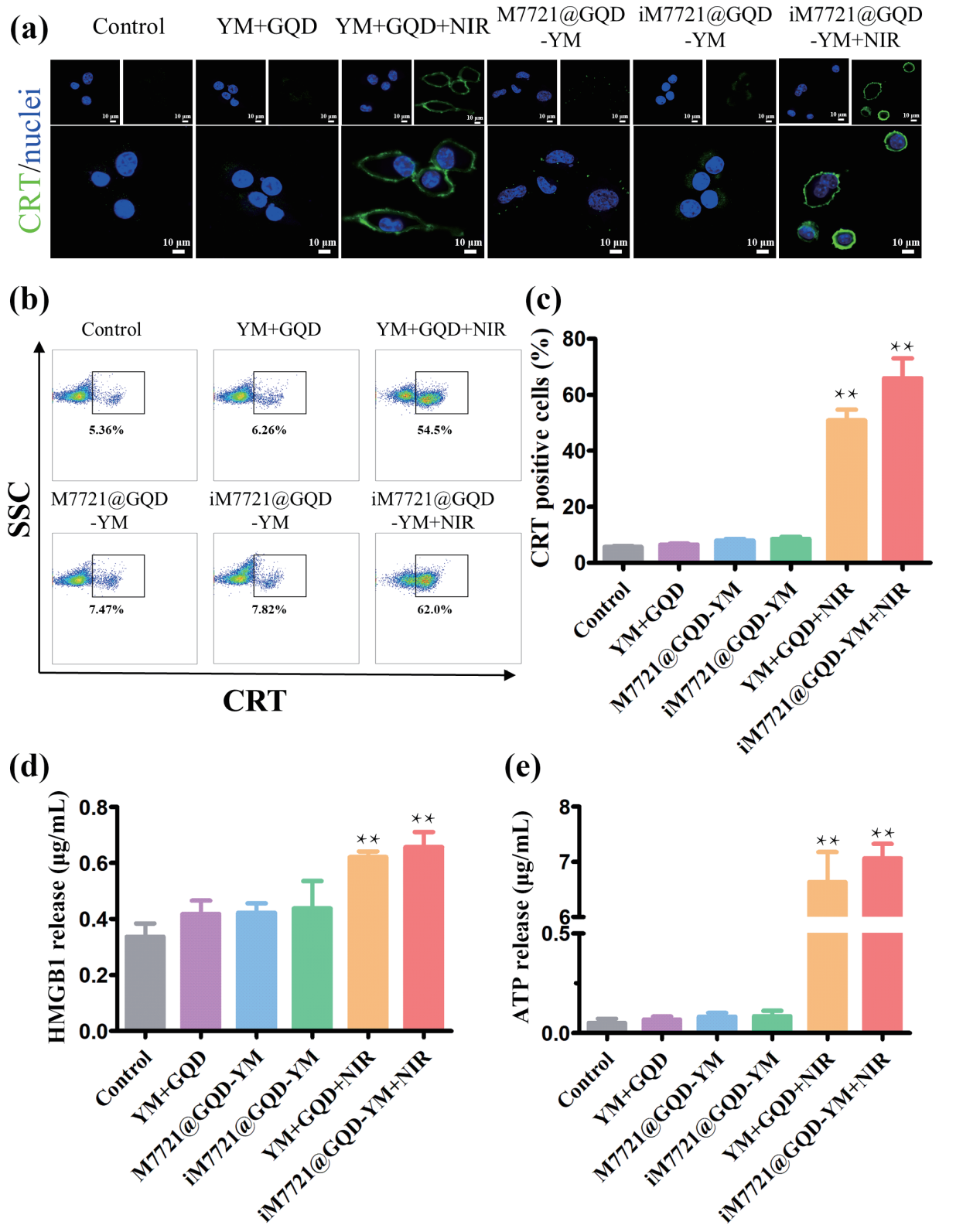

Figure 10 Hallmarks of ICD in biomimetic DDS treated cells. CLSM images (a) and FCM results ((b) and (c)) for surface expression of CRT on SMMC-7721 cells treated with iM7721@GQD-YM+NIR and counterparts. Green: CRT; blue: nucleus. HMGB1 (d) and ATP (e) release from SMMC-7721 cells treated with iM7721@GQD-YM+NIR and counterparts. $^{**}P < 0.01$.

characterized by measuring the temperature increase under NIR (LWIRPD-5F, Beijing Laserwave Opteolectronics Technology Co., Ltd., China) for different durations (808 nm, 0.8 W/cm^2). The temperature was measured by an IR thermal imaging system (E53, FLIR SYSTEMS AB, Sweden). Structure and spectral characteristics of NPs were measured by XRD (Rigaku Ultima IV, Japan), XPS (K-alpha, Thermo Scientific, USA), Raman spectrometer (Horiba evolution, Japan), FTIR (Nicolet AVATAR 370, Thermo Scientific, USA), and fluorescence spectrophotometer (Hitachi 7000, Japan), respectively. The ζ-potential, polydispersity index, hydrodynamic diameter, and size distribution of prepared samples were performed by ZetaSizer (Nano-ZS, Malvern Instruments, UK). The UV–vis absorption spectra were determined by a DU800 spectrophotometer (Beckman Coulter Inc, USA). SEM images were recorded using a Hitachi S-4800 FE-SEM.

3.7 *In vitro* drug release

A dialysis bag (molecular weight cut-off: 3.5 kDa) containing 2 mL iM7721@YM155 was put in a beaker containing 10 mL of PBS, which was fixed in a water bath to keep the temperature at 37 °C with continuous stirring. At various time points, 500 μL samples outside the dialysis bag were taken up and YM155 concentrations were measured using the UV–vis spectrum analysis at 252 nm absorbance. To detect the controlled release, samples were irradiated by 808 nm laser (1.0 W/cm^2) for 5 min before experiments.

3.8 *In vitro* cytotoxicity assessment

For cell counting kit-8 (CCK-8) analysis, cells were seeded into 96 well plates in 100 μL of culture medium supplemented with free and encapsulated YM155 with a gradient concentration from 0.5 to 16 μg/mL. For NIR groups, cells were irradiated with 808 nm laser (1.0 W/cm^2) for 5 min after 4 h of drug incubation. After 24 h of culture, 10 μL CCK-8 (Dojindo Molecular Technologies, Oslo, Norway) was respectively added to each well for another 2 h incubation in the dark. The absorbance (Ab) at 450 nm was recorded and the cell viability was calculated by the following function: $\text{Cellviability}\,(\%) = \frac{(\text{Ab}_{\text{Samples}} - \text{Ab}_{\text{Blank}})}{(\text{Ab}_{\text{Control}} - \text{Ab}_{\text{Blank}})} \times 100\%$, where Ab_{Blank} is the absorbance values of the culture medium without cells.

For live/dead staining, the prepared AM/PI cell double staining solution was added and incubated with cells in the incubator for 15 min according to the manufacturer's instructions, cells were then observed by CLSM (LSM 710, Zeiss, Germany).

3.9 Cellular uptake

Cellular uptake was observed by CLSM and quantitatively analyzed by flow cytometry (FCM). Cells were inoculated at a density of 5×10^4/well. After 24 h of culture, samples (free GQD, M8988@GQD, M7721@GQD, and iM7721@GQD) were added to each well with a final GQD concentration of 20 μg/mL for another 2 h-incubation. For CLAM, cells were washed and fixed by 4% paraformaldehyde at room temperature. After being stained with DAPI, cells were washed and subjected to confocal microscopic observation. For FCM, cells were collected, washed, and the fluorescence signal of GQD was analyzed by a Flow Cytometer (MoFlo XDPBD, Beckman Coulter, USA).

3.10 Cellular apoptosis assays

Cells in the logarithmic growth phase were prepared as a single-cell suspension and inoculated in 6-well plates at a density of 5 × 10^4/well. After 24 h, cells were treated with different formulations with the same YM155 concentration of 8 μg/mL for another 24 h. Cells of NIR group was irradiated with 808 nm laser (1.0 W/cm^2) for 5 min after 4 h drug treatment. Cells were then collected, washed with pre-cooled PBS, incubated with Annexin V-633 in the dark, and analyzed by FCM. Apoptotic cells were also observed by TEM measurement.

3.11 Western blotting

Cells were collected and suspended in lysis buffer containing protease and phosphatase inhibitors. The protein concentration was quantified by a BCA protein detection kit (Beyotime Biotechnology, Shanghai, China). Equal amount of protein samples was subjected to SDS-PAGE and immunoblotted with survivin or cleaved caspase-3/9 antibodies (Cell Signaling Technology, Massachusetts, USA).

3.12 *In vivo* studies

3.12.1 *Animals*

Four-week-old female BALB/c mice and SD rats were purchased from Slack Laboratory Animals Co., Ltd., Shanghai, China and housed in specific-pathogen-free (SPF) conditions. All the experiments on live mice were approved by the Committee on Animals of the Shanghai University (Shanghai, China). The experimental process was carried out in strict accordance with the care and Use Plan of Shanghai University Experimental Animal Institution (approved ECSHU-2020-030).

3.12.2 *Pharmacokinetic analysis*

SD rats (10-week-old) were randomly divided into two groups of 3 each, and jugular vein catheterization was employed for repeated blood sampling. Rats were administered tail vein injection of either free YM155 or iM7721@YM155, with an equivalent YM155 amount of 5 mg/kg. At each designated time points (5 min, 10 min, 15 min, 30 min, 1 h, 4 h, 8 h, 16 h, 24 h, and 48 h), approximately 150 μL of blood samples was collected in tubes containing EDTA as anticoagulant. Liquid chromatographytandem mass spectrometry (LC-MS/MS) was employed to determine the plasma concentration of YM155 [53]. The data were analyzed by PK solver software.

3.12.3 *In vivo biodistribution and photothermal effect*

Tumor bearing mice were randomly divided into different groups and intravenously injected with iM7721@GQD or the counterparts. For *in vivo* biodistribution analysis, the cytomembrane carriers were labeled with cell membrane dye DiD before injection. Mice were anesthetized at different time points post injection, and the fluorescence imaging was performed by IVIS Lumina III imaging system (PerkinElmer, California, USA). Finally, mice were euthanized, the tumors and main organs were obtained and analyzed by IVIS Lumina III in a Vivo imaging system. For *in vivo* photothermal evaluation, the tumor sites of nude mice were irradiated by NIR (1 W/cm^2, 5 min) 12 h post injection, and the temperature alteration was recorded by a thermal infrared imaging system.

3.12.4 *Treatment of established tumors in vivo*

SMMC-7721 cells (2 × 10^7) suspended in 200 μL PBS was inoculated subcutaneously into the lateral flank of 5-week-old BAL B/c nude mice. When tumors reached about 8 mm in length, mice were randomly divided into 6 groups and respectively administered with tail vein injection of (a) PBS, (b) free YM155 and GQD, (c) M7721@GQD-YM, (d) iM7721@GQD-YM, (e) YM155+GQD+NIR, and (f) iM7721@GQD-YM+NIR with an equal amount of YM155 (5 mg/kg) every three days for three times. For irradiated groups, mice were irradiated with NIR (808 nm, 1 W/cm^2) for 5 min 12 h post treatment. The tumor size was measured in two perpendicular diameters with precision calipers every three days and calculated according to the following equation: $\text{Tumor volume} = \frac{L \times W^2}{2}$ (L: tumor length; W: tumor width).

All mice were euthanized on day 21 after treatment and dissected to obtain tumors and vital organs. Tissues were fixed with 4% paraformaldehyde for H&E staining, Ki-67 immunohistochemical staining, HSP immunofluorescence staining, and TUNEL. For survival analysis, mice were observed daily until natural death in a range of 40 days.

3.13 Detection of surface CRT expression

For CLSM evaluation, SMCC-7721 cells were inoculated in a

35 mm Petri laser confocal culture dish at a density of 5 × 10^4 cells/well overnight and subjected with different treatments. After being fixed with 4% paraformaldehyde, cells were stained with anti-CRT antibody, Alexa Fluor 488 labeled secondary antibody, and DAPI in succession in the dark. Cells were then observed by CLSM. For FCM analysis, cells were seeded in 6-well plates and subjected with different treatments for 20 h. Cells were collected, washed with PBS, labeled with anti-CRT antibodies for 2 h, and then analyzed by a Flow Cytometer.

3.14 Detection of extracellular release of HMGB1 and ATP

SMMC-7721 cells were seeded in 6-well plates and subjected with different treatments for 20 h. Then the cell supernatants were collected and the contents of HMGB1 and ATP were detected according to the instructions of HMGB1 ELISA kit (Fine Biotech Co. Ltd., Wuhan, China) and ATP detection kit (Beyotime Biotech Co. Ltd., Shanghai, China).

3.15 Statistical analysis

Results have been reported in this study as means ± standard deviations (sd). Statistical analysis was performed by Student's unpaired *t*-test or one-way analysis of variance (ANOVA) to identify significant differences unless otherwise indicated. Differences were considered significant when $p < 0.05$.

4 Conclusions

In this study, a novel nano-drug delivery system iM7721@GQD-YM was successfully constructed by biomimetic strategy. SMMC-7721 cell membrane coating endowed iM7721@GQD-YM with effective targeting ability to homologous cells, and excellent biocompatibility & immunocompatibility for *in vivo* application. Surface decoration of iRGD further enhanced its tumor targeting activity by iRGD-integrin recognition between biomimetic NPs and target cells. In addition, under NIR irradiation, GQD can directly kill tumors through photothermal effect, and cause cell membrane rupture, accurately releasing survivin inhibitor YM155 at tumor sites. In addition, immunogenic cell death can also be detected in malignant cells treated with iM7721@GQD-YM and NIR irradiation. In conclusion, the versatile biomimetic DDS hold great potential for the treatment of homologous HC, which merits further investigation in both pre-clinical and clinical studies.

Acknowledgments

This work was sponsored by "One Belt One Road" International Cooperation Project of Shanghai Municipal Committee of Science and Technology (No. 19410740900), the National Natural Science Foundation of China (No. 52002239), the International Science and Technology Cooperation Programme of Ministry of Science and Technology of China (No. 2019YFE0116800), and Natural Science Foundation of Shanghai (No. 21ZR1422800).

Electronic Supplementary Material: Supplementary material (some additional experimental data being helpful to support the conclusions of this study) is available in the online version of this article at https://doi.org/10.1007/s12274-022-4462-8.

References

[1] Sung, H.; Ferlay, J.; Siegel, R. L.; Laversanne, M.; Soerjomataram, I.; Jemal, A.; Bray, F. Global cancer statistics 2020: GLOBOCAN estimates of incidence and mortality worldwide for 36 cancers in 185 countries. *CA Cancer J. Clin.* **2021**, *71*, 209–249.

[2] McGlynn, K. A.; Petrick, J. L.; El-Serag, H. B. Epidemiology of hepatocellular carcinoma. *Hepatology* **2021**, *73 Suppl 1*, 4–13.

[3] Anwanwan, D.; Singh, S. K.; Singh, S.; Saikam, V.; Singh, R. Challenges in liver cancer and possible treatment approaches. *Biochim. Biophys. Acta Rev. Cancer* **2020**, *1873*, 188314.

[4] Lee, Y. T.; Wang, J. J.; Luu, M.; Noureddin, M.; Kosari, K.; Agopian, V. G.; Rich, N. E.; Lu, S. C.; Tseng, H. R.; Nissen, N. N. et al. The mortality and overall survival trends of primary liver cancer in the United States. *J. Natl. Cancer Inst.* **2021**, *113*, 1531–1541.

[5] Siegel, R. L.; Miller, K. D.; Fuchs, H. E.; Jemal, A. Cancer statistics, 2021. *CA Cancer J. Clin.* **2021**, *71*, 7–33.

[6] Martínez-García, D.; Manero-Rupérez, N.; Quesada, R.; Korrodi-Gregório, L.; Soto-Cerrato, V. Therapeutic strategies involving survivin inhibition in cancer. *Med. Res. Rev.* **2019**, *39*, 887–909.

[7] Jiang, X. Y.; Wilford, C.; Duensing, S.; Munger, K.; Jones, G.; Jones, D. Participation of survivin in mitotic and apoptotic activities of normal and tumor-derived cells. *J. Cell. Biochem.* **2001**, *83*, 342–354.

[8] Min, L. H.; Ji, Y.; Bakiri, L.; Qiu, Z. X.; Cen, J.; Chen, X. T.; Chen, L. L.; Scheuch, H.; Zheng, H.; Qin, L. X. et al. Liver cancer initiation is controlled by AP-1 through SIRT6-dependent inhibition of survivin. *Nat. Cell Biol.* **2012**, *14*, 1203–1211.

[9] Su, C. Q. Survivin in survival of hepatocellular carcinoma. *Cancer Lett.* **2016**, *379*, 184–190.

[10] Santarelli, A.; Mascitti, M.; Lo Russo, L.; Sartini, D.; Troiano, G.; Emanuelli, M.; Lo, M. L. Survivin-based treatment strategies for squamous cell carcinoma. *Int. J. Mol. Sci.* **2018**, *19*, 971.

[11] Sumi, T.; Hirai, S.; Yamaguchi, M.; Tanaka, Y.; Tada, M.; Yamada, G.; Hasegawa, T.; Miyagi, Y.; Niki, T.; Watanabe, A. et al. Survivin knockdown induces senescence in TTF-1-expressing, KRAS-mutant lung adenocarcinomas. *Int. J. Oncol.* **2018**, *53*, 33–46.

[12] Gundamaraju, R.; Vemuri, R.; Chong, W. C.; Myers, S.; Norouzi, S.; Shastri, M. D.; Eri, R. Interplay between endoplasmic reticular stress and survivin in colonic epithelial cells. *Cells* **2018**, *7*, 171.

[13] Nyquist, M. D.; Corella, A.; Burns, J.; Coleman, I.; Gao, S.; Tharakan, R.; Riggan, L.; Cai, C. M.; Corey, E.; Nelson, P. S. et al. Exploiting AR-regulated drug transport to induce sensitivity to the survivin inhibitor YM155. *Mol. Cancer Res.* **2017**, *15*, 521–531.

[14] Nakahara, T.; Kita, A.; Yamanaka, K.; Mori, M.; Amino, N.; Takeuchi, M.; Tominaga, F.; Kinoyama, I.; Matsuhisa, A.; Kudou, M. et al. Broad spectrum and potent antitumor activities of YM155, a novel small-molecule Survivin suppressant, in a wide variety of human cancer cell lines and xenograft models. *Cancer Sci.* **2011**, *102*, 614–621.

[15] Nakahara, T.; Takeuchi, M.; Kinoyama, I.; Minematsu, T.; Shirasuna, K.; Matsuhisa, A.; Kita, A.; Tominaga, F.; Yamanaka, K.; Kudoh, M. et al. YM155, a novel small-molecule survivin suppressant, induces regression of established human hormone-refractory prostate tumor xenografts. *Cancer Res.* **2007**, *67*, 8014–8021.

[16] Wang, C. L.; Zhang, W.; He, Y. J.; Gao, Z. R.; Liu, L. Y.; Yu, S. Y.; Hu, Y. X.; Wang, S.; Zhao, C. C.; Li, H. et al. Ferritin-based targeted delivery of arsenic to diverse leukaemia types confers strong anti-leukaemia therapeutic effects. *Nat. Nanotechnol.* **2021**, *16*, 1413–1423.

[17] Bao, W. E.; Liu, M.; Meng, J. Q.; Liu, S. Y.; Wang, S.; Jia, R. R.; Wang, Y. G.; Ma, G. H.; Wei, W.; Tian, Z. Y. MOFs-based nanoagent enables dual mitochondrial damage in synergistic antitumor therapy via oxidative stress and calcium overload. *Nat. Commun.* **2021**, *12*, 6399.

[18] Feng, S. N.; Ren, Y. J.; Li, H.; Tang, Y. F.; Yan, J. Y.; Shen, Z. Y.; Zhang, H. J.; Chen, F. X. Cancer cell-membrane biomimetic boron nitride nanospheres for targeted cancer therapy. *Int. J. Nanomedicine* **2021**, *16*, 2123–2136.

[19] Wang, C.; Jiang, Y.; Ma, J. M.; Wu, H. X.; Wacker, D.; Katritch, V.; Han, G. W.; Liu, W.; Huang, X. P.; Vardy, E. et al. Structural basis for molecular recognition at serotonin receptors. *Science* **2013**, *340*, 610–614.

[20] Li, H. F.; Jin, H.; Wan, W.; Wu, C.; Wei, L. X. Cancer

nanomedicine: Mechanisms, obstacles and strategies. *Nanomedicine (Lond)* **2018**, *13*, 1639–1656.
[21] Yang, Y. Y.; Yu, Y. J.; Chen, H.; Meng, X. X.; Ma, W.; Yu, M.; Li, Z. Y.; Li, C. H.; Liu, H. L.; Zhang, X. D. et al. Illuminating platinum transportation while maximizing therapeutic efficacy by gold nanoclusters via simultaneous near-infrared-I/II imaging and glutathione scavenging. *ACS Nano* **2020**, *14*, 13536–13547.
[22] Zhong, W. H.; Zhang, X. Y.; Zeng, Y. X.; Lin, D. J.; Wu, J. Recent applications and strategies in nanotechnology for lung diseases. *Nano Res.* **2021**, *14*, 2067–2089.
[23] Sun, H. P.; Su, J. H.; Meng, Q. S.; Yin, Q.; Chen, L. L.; Gu, W. W.; Zhang, P. C.; Zhang, Z. W.; Yu, H. J.; Wang, S. L. et al. Cancer-cell-biomimetic nanoparticles for targeted therapy of homotypic tumors. *Adv. Mater.* **2016**, *28*, 9581–9588.
[24] Hu, C. M. J.; Fang, R. H.; Wang, K. C.; Luk, B. T.; Thamphiwatana, S.; Dehaini, D.; Nguyen, P.; Angsantikul, P.; Wen, C. H.; Kroll, A. V. et al. Nanoparticle biointerfacing by platelet membrane cloaking. *Nature* **2015**, *526*, 118–121.
[25] Gong, H.; Zhang, Q. Z.; Komarla, A.; Wang, S. Y.; Duan, Y. O.; Zhou, Z. D.; Chen, F.; Fang, R. H.; Xu, S.; Gao, W. W. et al. Nanomaterial biointerfacing via mitochondrial membrane coating for targeted detoxification and molecular detection. *Nano Lett.* **2021**, *21*, 2603–2609.
[26] Fan, Z. Y.; Li, P. Y.; Deng, J. J.; Bady, S. C.; Cheng, H. Cell membrane coating for reducing nanoparticle-induced inflammatory responses to scaffold constructs. *Nano Res.* **2018**, *11*, 5573–5583.
[27] Zhu, J. Y.; Zheng, D. W.; Zhang, M. K.; Yu, W. Y.; Qiu, W. X.; Hu, J. J.; Feng, J.; Zhang, X. Z. Preferential cancer cell self-recognition and tumor self-targeting by coating nanoparticles with homotypic cancer cell membranes. *Nano Lett.* **2016**, *16*, 5895–5901.
[28] Chai, Z. L.; Ran, D. N.; Lu, L. W.; Zhan, C. Y.; Ruan, H. T.; Hu, X. F.; Xie, C.; Jiang, K.; Li, J. Y.; Zhou, J. F. et al. Ligand-modified cell membrane enables the targeted delivery of drug nanocrystals to glioma. *ACS Nano* **2019**, *13*, 5591–5601.
[29] Liu, W.; Ruan, M. L.; Wang, Y. M.; Song, R. G.; Ji, X.; Xu, J. K.; Dai, J.; Xue, W. Light-triggered biomimetic nanoerythrocyte for tumor-targeted lung metastatic combination therapy of malignant melanoma. *Small* **2018**, *14*, e1801754.
[30] Liu, X. J.; Sun, Y. X.; Xu, S. S.; Gao, X. N.; Kong, F. P.; Xu, K. H.; Tang, B. Homotypic cell membrane-cloaked biomimetic nanocarrier for the targeted chemotherapy of hepatocellular carcinoma. *Theranostics* **2019**, *9*, 5828–5838.
[31] Luo, Z. Q.; Weiss, D. E.; Liu, Q. Y.; Tian, B. Z. Biomimetic approaches toward smart bio-hybrid systems. *Nano Res.* **2018**, *11*, 3009–3030.
[32] Gao, J. B.; Wang, F.; Wang, S. H.; Liu, L.; Liu, K.; Ye, Y. C.; Wang, Z.; Wang, H.; Chen, B.; Jiang, J. M. et al. Hyperthermia-triggered on-demand biomimetic nanocarriers for synergetic photothermal and chemotherapy. *Adv. Sci. (Weinh.)* **2020**, *7*, 1903642.
[33] Obaid, G.; Samkoe, K.; Tichauer, K.; Bano, S.; Park, Y.; Silber, Z.; Hodge, S.; Callaghan, S.; Guirguis, M.; Mallidi, S. et al. Is tumor cell specificity distinct from tumor selectivity *in vivo*?: A quantitative NIR molecular imaging analysis of nanoliposome targeting. *Nano Res.* **2021**, *14*, 1344–1354.
[34] Geng, B. J.; Shen, W. W.; Fang, F. L.; Qin, H.; Li, P.; Wang, X. L.; Li, X. K.; Pan, D. Y.; Shen, L. X. Enriched graphitic N dopants of carbon dots as F cores mediate photothermal conversion in the NIR-II window with high efficiency. *Carbon* **2020**, *162*, 220–233.
[35] Ren, Y. J.; Miao, C. L.; Tang, L.; Liu, Y. X.; Ni, P. Y.; Gong, Y.; Li, H.; Chen, F. X.; Feng, S. N. Homotypic cancer cell membranes camouflaged nanoparticles for targeting drug delivery and enhanced chemo-photothermal therapy of glioma. *Pharmaceuticals (Basel)* **2022**, *15*, 157.
[36] Li, H. F.; Wu, C.; Xia, M.; Zhao, H.; Zhao, M. X.; Hou, J.; Li, R.; Wei, L. X.; Zhang, L. Targeted and controlled drug delivery using a temperature and ultra-violet responsive liposome with excellent breast cancer suppressing ability. *RSC Adv.* **2015**, *5*, 27630–27639.
[37] Bhagat, M.; Sofou, S. Membrane heterogeneities and fusogenicity in phosphatidylcholine-phosphatidic acid rigid vesicles as a function of pH and lipid chain mismatch. *Langmuir* **2010**, *26*, 1666–1673.
[38] Kanehisa, M. I.; Tsong, T. Y. Cluster model of lipid phase transitions with application to passive permeation of molecules and structure relaxations in lipid bilayers. *J. Am. Chem. Soc.* **1978**, *100*, 424–432.
[39] Sung, S. Y.; Su, Y. L.; Cheng, W.; Hu, P. F.; Chiang, C. S.; Chen, W. T.; Hu, S. H. Graphene quantum dots-mediated theranostic penetrative delivery of drug and photolytics in deep tumors by targeted biomimetic nanosponges. *Nano Lett.* **2019**, *19*, 69–81.
[40] Zhang, L. J.; Zhang, X.; Lu, G. H.; Li, F.; Bao, W. E.; Song, C.; Wei, W.; Ma, G. H. Cell membrane camouflaged hydrophobic drug nanoflake sandwiched with photosensitizer for orchestration of chemo-photothermal combination therapy. *Small* **2019**, *15*, e1805544.
[41] Chen, G.; Yang, Y. Y.; Xu, Q.; Ling, M. J.; Lin, H. M.; Ma, W.; Sun, R.; Xu, Y. C.; Liu, X. Q.; Li, N. et al. Self-amplification of tumor oxidative stress with degradable metallic complexes for synergistic cascade tumor therapy. *Nano Lett.* **2020**, *20*, 8141–8150.
[42] Hao, H. S.; Chen, Y.; Wu, M. Y. Biomimetic nanomedicine toward personalized disease theranostics. *Nano Res.* **2021**, *8*, 2491–2511.
[43] Jiang, Y.; Krishnan, N.; Zhou, J. R.; Chekuri, S.; Wei, X. L.; Kroll, A. V.; Yu, C. L.; Duan, Y. O.; Gao, W. W.; Fang, R. H. et al. Engineered cell-membrane-coated nanoparticles directly present tumor antigens to promote anticancer immunity. *Adv. Mater.* **2020**, *32*, e2001808.
[44] Liu, M. T.; Ma, W. J.; Zhao, D.; Li, J. J.; Li, Q. R.; Liu, Y. H.; Hao, L. Y.; Lin, Y. F. Enhanced penetrability of a tetrahedral framework nucleic acid by modification with iRGD for DOX-targeted delivery to triple-negative breast cancer. *ACS Appl. Mater. Interfaces* **2021**, *13*, 25825–25835.
[45] Gholizadeh, S.; Dolman, E. M.; Wieriks, R.; Sparidans, R. W.; Hennink, W. E.; Kok, R. J. Anti-GD2 immunoliposomes for targeted delivery of the survivin inhibitor sepantronium bromide (YM155) to neuroblastoma tumor cells. *Pharm. Res.* **2018**, *35*, 85.
[46] Schmitt, E.; Gehrmann, M.; Brunet, M.; Multhoff, G.; Garrido, C. Intracellular and extracellular functions of heat shock proteins: Repercussions in cancer therapy. *J. Leukoc. Biol.* **2007**, *81*, 15–27.
[47] Duan, X. P.; Chan, C.; Lin, W. B. Nanoparticle-mediated immunogenic cell death enables and potentiates cancer immunotherapy. *Angew. Chem., Int. Ed.* **2019**, *58*, 670–680.
[48] Gupta, G.; Borglum, K.; Chen, H. X. Immunogenic cell death: A step ahead of autophagy in cancer therapy. *J. Cancer Immunol. (Wilmington)* **2021**, *3*, 47–59.
[49] Evans, S. S.; Repasky, E. A.; Fisher, D. T. Fever and the thermal regulation of immunity: The immune system feels the heat. *Nat. Rev. Immunol.* **2015**, *15*, 335–349.
[50] Geng, B. J.; Shen, W. W.; Li, P.; Fang, F. L.; Qin, H.; Li, X. K.; Pan, D. Y.; Shen, L. X. Carbon dot-passivated black phosphorus nanosheet hybrids for synergistic cancer therapy in the NIR-II window. *ACS Appl. Mater. Interfaces* **2019**, *11*, 44949–44960.
[51] Chen, H. L.; Zheng, D. H.; Pan, W. Z.; Li, X.; Lv, B.; Gu, W. X.; Machuki, J. O.; Chen, J. H.; Liang, W. Q.; Qin, K. et al. Biomimetic nanotheranostics camouflaged with cancer cell membranes integrating persistent oxygen supply and homotypic targeting for hypoxic tumor elimination. *ACS Appl. Mater. Interfaces* **2021**, *13*, 19710–19725.
[52] Gao, W. W.; Hu, C. M. J.; Fang, R. H.; Luk, B. T.; Su, J.; Zhang, L. F. Surface functionalization of gold nanoparticles with red blood cell membranes. *Adv. Mater.* **2013**, *25*, 3549–3553.
[53] Dolman, M. E. M.; den Hartog, I. J. M.; Molenaar, J. J.; Schellens, J. H. M.; Beijnen, J. H.; Sparidans, R. W. Liquid chromatography-tandem mass spectrometric assay for the light sensitive Survivin suppressant sepantronium bromide (YM155) in mouse plasma. *J. Pharm. Biomed. Anal.* **2014**, *92*, 144–148.